Soft Matter

PAPER

View Article Online
View Journal | View Issue

Cite this: *Soft Matter*, 2020, **16**, 5506

Aggregation in viscoelastic emulsion droplet gels with capillarity-driven rearrangements

Abigail Thiel,[a] Timothy J. Atherton,[b] Patrick T. Spicer *[c] and Richard W. Hartel[a]

Received 27th October 2019,
Accepted 20th May 2020

DOI: 10.1039/c9sm02134e

rsc.li/soft-matter-journal

Arrested, or partial, coalescence of viscoelastic emulsion droplets can occur when elastic resistance to deformation offsets droplet surface area minimization. Arrest is a critical element of food and consumer product microstructure and performance, but direct studies of structural arrest and rearrangement have been carried out using only two or three droplets at a time. The question remains whether the behavior of small numbers of droplets also occurs in larger, more realistic many-droplet systems. Here we study two-dimensional aggregation and arrested coalescence of emulsions containing ~1000 droplets and find that the restructuring mechanisms observed for smaller systems have a large effect on local packing in multidroplet aggregates, but surprisingly do not significantly alter overall mass scaling in the aggregates. Specifically, increased regions of hexagonal packing are observed as the droplet solids level, and thus elasticity, is decreased because greater degrees of capillary force-driven restructuring are possible. Diffusion-limited droplet aggregation simulations that account for the restructuring mechanisms agree with the experimental results and suggest a basis for prediction of larger-scale network properties and bulk emulsion behavior.

1 Introduction

Emulsion droplets are the basis for the texture and quality of numerous food and industrial products, so their microstructure and stability are critical control variables[1–3] in need of optimization. Droplets without added emulsifiers can coalesce into a single, larger droplet, destabilizing an emulsion, while added emulsifiers can prevent coalescence. Between these two extremes is the case when droplets have some inherent elastic resistance to interfacial tension-induced coalescence. For such viscoelastic emulsion droplets, coalescence can initiate but then be arrested before completion by internal or surface elasticity. The magnitude of the elastic stress a droplet can bear is determined by its solid content, setting the degree to which two droplets that have started to merge can resist further deformation.

The arrested droplet concept in food emulsions[4,5] inspired applications in the field of consumer products, where it was recognized that the internal viscoelasticity of droplets can preserve non-spherical and advantageous shapes,[6] enable responsiveness to external stimuli,[7,8] and enhance deposition onto biological surfaces.[9,10] Other envisioned applications of arrested droplets are as a basis for hierarchical microstructures in microfluidic-generated[11,12] or 3D-printed[13] advanced materials.

A number of studies have examined the arrested coalescence of partially crystalline emulsions at the length scale of droplets. One work developed a simple physical model that describes arrest of droplet pairs during coalescence, balancing droplet elasticity with interfacial Laplace pressure to determine the final configuration.[14] The result is descriptive of same-sized and different-sized petrolatum droplet pairs,[15] as well as droplets containing mixtures of milkfat.[16] As soon as a third droplet is added to a pair, however, the loss of symmetry significantly increases the complexity of arrested coalescence, Fig. 1. Depending on the angle of approach of the new droplet, the free fluid in the initial droplet pair can cause rearrangement from the initial collision state into close packing.[17]

Ultimately the bulk microstructure of arrested many-droplet networks determines a material's mechanical response, as in waxy crude oil emulsions,[18] as well as effects on perception, appearance, and nutrition of products like butter, whipped cream, and ice cream.[19] Past work on arrested emulsion microstructures studied bulk mechanical[20–22] or structural properties[23,24] without the benefit of recent insights into droplet-scale arrest dynamics.[14,17,25] However, those droplet-scale results have similarly not been tested for applicability during formation of larger-scale networks.

All of the above applications rely on the creation of an emulsion gel structure, but if rearrangement mechanisms affect the process, reproducible manufacturing of a desired structure could be difficult. While restructuring is known to occur in solid particle dispersions, leading to more dense

[a] *Department of Food Science, University of Wisconsin-Madison, Madison, WI, USA*
[b] *Department of Physics and Astronomy, Tufts University, Boston, MA, USA*
[c] *School of Chemical Engineering, UNSW Sydney, NSW, Australia.*
E-mail: p.spicer@unsw.edu.au

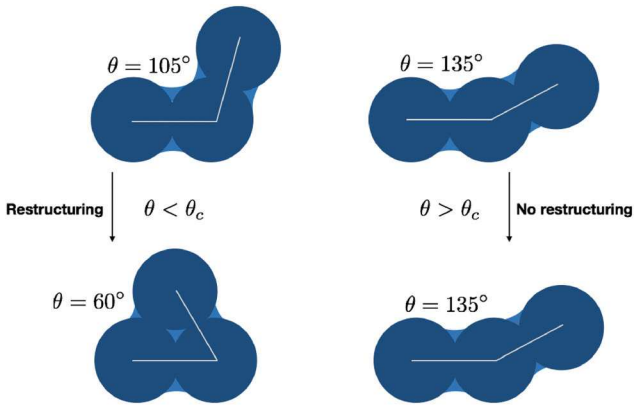

Fig. 1 Schematic of the basis for the simulated aggregation study showing aggregates containing a lighter-colored fluid meniscus in between darker, more elastic, spherical structures. A diffusion-limited aggregation simulation is performed with an additional criterion that droplets will rotate, or restructure, into a closer-packed state if their approach angle, θ, exceeds a critical value of θ_c, here 120°. Restructuring occurs through the capillary action of the light blue fluid meniscus and is only possible when the two menisci forming necks between arrested droplets overlap during the initial coalescence approach.[17]

fractal packing than from aggregation alone,[26–28] arrested droplet gels and their rheology-capillarity dynamics have been examined far less. One recent outstanding experimental work examined arrested coalescence of droplets during heating,[29] finding clear evidence of restructured clusters and emphasizing the need to study larger-scale emulsions experiencing flow. This latter challenge is the focus of this paper.

Here we study many-droplet network formation on a surface *via* flow-induced arrested coalescence and capillary-driven rearrangements. Experimental characterization of the fractal droplet networks demonstrates that droplet rearrangement leads to localized increases in packing density but, surprisingly, the final fractal structure is not strongly affected. A simulation of the droplet aggregation and rearrangement processes agrees well with experimental trends, identifying droplet coordination number and bond angle as key structural signatures of rearrangement. We anticipate these observations can begin to inform large-scale simulation of arrested emulsion gel formation, building on the valuable insights gained from recent models of colloidal gelation,[30] structural rearrangement,[31,32] and yielding.[33] As the restructuring mechanisms studied here can occur even in non-Brownian systems, the potential exists to broaden the applicability of self-assembly processes for structure development.[34] More realistic structural models could greatly accelerate design and optimization of novel forms of foods, pharmaceuticals, and additive manufactured products.

2 Methods and materials

Different ratios of paraffin (H&R GSP Pty. Ltd) and hexadecane (99%, Sigma) were combined to produce an oil–wax mixture with the desired solids level, between 25% w/w and 70% solid wax. The oil phase was then added to water to produce an emulsion with 5% w/w dispersed phase. The emulsion was heated at 60 °C for 10 min and then shaken by hand for 5 s to disperse the oil droplets. The emulsion cools quickly and the wax solidifies to create the viscoelasticity under study here. At the lower solids levels, there is a smaller driving force for crystallization and some total coalescence can occur before crystallization is complete. A slight increase in primary droplet size in those emulsions occurs, but does not affect the results.

A volume of emulsion was directly pipetted onto glass slides and time allowed for the oil droplets to migrate to the top of the total liquid volume as a result of buoyancy. The Bond number indicates the dominant contribution to emulsion droplet position is interfacial, as $\mathrm{Bo} = \frac{\rho g d^2}{\gamma} \sim 10^{-3}$, where ρ is the droplet density, g is the gravitational acceleration, d is droplet diameter, and γ is the air–water surface tension. A large group of close-packed oil droplets gathers near the peak of the water–air interface, Fig. 2A. The volume fraction of the emulsion just before aggregation initiates is clearly that of a nearly close-packed polydisperse emulsion, as shown in Fig. 2A. The oil droplets at the outer edge of the group exert pressure on the inner droplets because of the oil droplet buoyancy, and finally cause a droplet network to rapidly form, Fig. 2B, and then slide down the top edge of the water droplet to settle near its edge, Fig. 2C. All the water is then slowly evaporated, over the course of 8 hours, gently placing the arrested droplet network on the glass slide surface and allowing single-plane imaging. Fig. 2C shows a view of a droplet network that has formed on the air–water interface prior to drying and final imaging. These views were used to verify that the droplet aggregate structure is now structurally stable and does not change during the drying

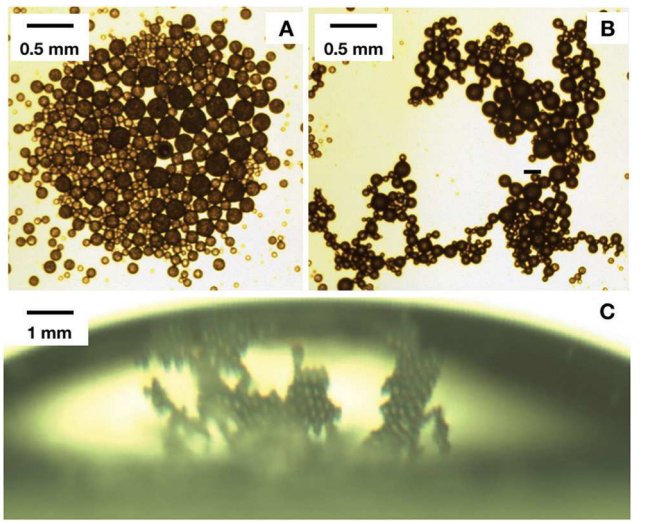

Fig. 2 Droplet network formation on water droplet surface. (A) Viewed from above, a sessile water droplet gathers oil droplets on its top as a result of buoyancy forces. The droplets eventually begin to coalesce as the force pushing them together overcomes viscous resistance. (B) Droplet networks form as the droplet coalescence is arrested by the internal elastic microstructure of the droplets. (C) Side view of droplet networks prior to drying and in-plane imaging.

process by comparison with final images. Observation and imaging of the droplet networks is then performed using a Motic AE31 inverted microscope. The size distribution of the emulsion was quantified by image analysis and found to be log-normally distributed, as is common for dispersed systems, with a geometric mean diameter of 70 μm. The coordinates of the centers of mass of each droplet within a network were determined *via* image analysis with ImageJ.[35]

3 Results and discussion

Droplet aggregates observed in previous studies[29] strongly resemble the dendritic structures formed by the well-studied process of diffusion-limited aggregation (DLA).[36] As the solid fraction is lowered, however, the structure increasingly incorporates crystalline—*i.e.* hexagonally coordinated—regions, while intriguingly retaining an aggregate-like structure at larger length scales.[29] In pioneering studies of DLA,[37–40] the fractal nature of aggregates was shown through a non-integer power-law decay of mass as a function of distance from the center of the aggregate. Following this work, the effect of large-scale reorganization was shown to be able to modify the observed fractal dimension of the cluster.[41] In contrast, the reorganization process we expect is operative only on droplets as they join the cluster.

In previous work, we investigated the assembly of triplets of emulsion droplets,[17] finding that capillary interactions move a droplet that joins a host doublet to close-pack with the first two if the approach angle is less than some critical value θ_c, Fig. 1. The angle represents the point at which the menisci between pairs of droplets just touch; below θ_c global minimization of the contact area between the emulsion fluid and the continuous phase increases the packing density of the droplet cluster.

To understand the effect of this process on a DLA structure, we performed the following simulation: aggregates grow one particle at a time from an initial seed particle with the single free particle moving by a continuous random walk, of step size ξ, until it collides with a particle already in the aggregate. Upon contact, the existing neighbors of the contact particle are determined and, if the new particle is less than an angular distance θ_c from one of them, it is moved into contact with the nearest neighbor. The process continues until N particles have been added.

Aggregates grown with N = 3000 are shown in Fig. 3A for several values of θ_c. As θ_c increases, more collisions result in rearrangement, so the aggregates increasingly incorporate close-packed regions. At the limiting value of $\theta_c = \pi$, the branches are significantly thickened from the $\theta_c = 0$ case. To quantitatively examine the structure, the density–density correlation function, $g(r)$, is shown in Fig. 3B for several

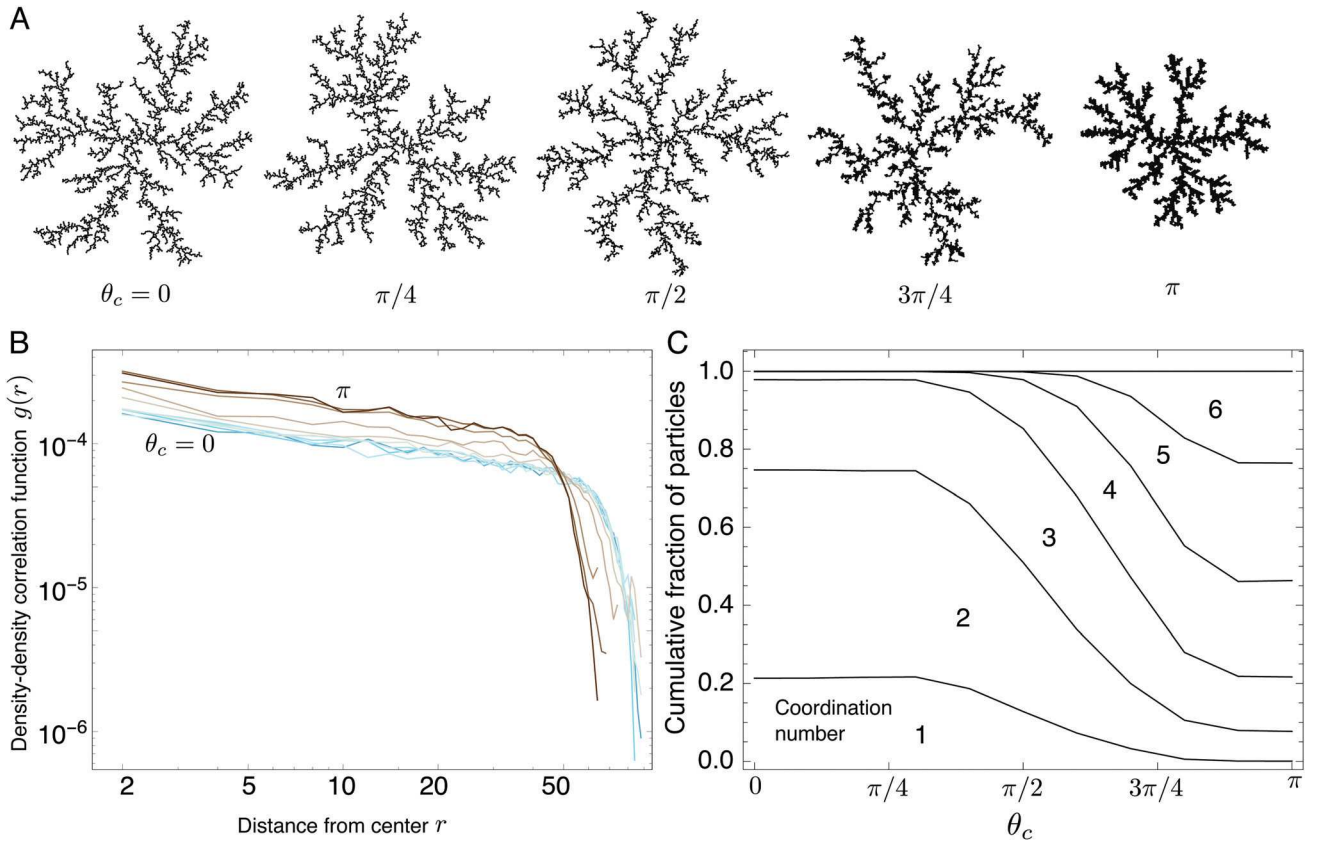

Fig. 3 Simulated aggregates. Diffusion-limited aggregation with internal rearrangements at the time of contact. (A) Representative aggregates with N = 3000 particles for different values of θ_c. (B) Density–density correlation function $g(r)$ for an ensemble of aggregates. (C) Fraction of particles with different coordination numbers as a function of θ_c.

values of θ_c. Each has the characteristic structure described in ref. 37, *i.e.*, a power-law decrease in $g(r) \propto r^{\alpha}$ for $r < r_c$. Here r_c is roughly the radius of the aggregate; above r_c, $g(r)$ vanishes rapidly. The value of the exponent remarkably does not depend on θ_c as may be crudely observed from Fig. 3B since the linear portions of the plots are all parallel. The fitted value $\alpha = 0.34 \pm 0.005$ is entirely consistent with traditional DLA results.[37] This is in contrast to large-scale reorganization, which does tend to change the scaling exponent.

While the reorganization process does not affect the macroscopic fractal structure of the aggregate, the local environment of the droplets is significantly modified. In Fig. 3C, the fraction of particles with different coordination numbers is shown as a function of θ_c. For low θ_c, most particles have 2 neighbors, with a much smaller number having 1 or 3. The distribution is unchanged until $\theta_c \gtrsim \pi/4$, where the fraction of doubly coordinated particles drops sharply with an increasing population of 4-, 5- and 6-fold coordinated particles appearing.

Fig. 2 shows an example of an experimental formation of two-dimensional partially crystalline emulsion droplet aggregates on the surface of a water droplet. The curved interface directs the emulsion droplets to assemble into larger structures[42] as a result of their buoyancy, Fig. 2A. After coalescence initiates, it rapidly propagates[29] through the droplet group to form irregular fractal structures, Fig. 2B. The rapid formation of the networks prevents direct observation of the process, but we compare to our simulation results by study of their final structures.

Fig. 4 shows micrographs of droplet networks formed at solids levels varying from 25% to 70% solid paraffin. All drop networks are in various states of arrested coalescence or aggregation and the images were examined to quantify the aggregate structures. Consistent with earlier work on arrested coalescence of droplet pairs,[14] the deformation of the resultant droplets decreases with increasing solids level. Above 40% solids, the droplets do not significantly deform as a result of the Laplace pressure on the interface, and so are not arrested but aggregated. Nevertheless, the aggregation occurs due to a small wetting film between droplets, unlike attractive colloids or adhesive emulsions.[43,44] The fluid meniscus also determines whether the droplet is restructured into a close-packed state after collision.[17] Drops added to more deformable, or lower solids-containing, droplet pairs had a higher probability of restructuring. All other variables held constant, we expect droplets containing lower solids levels to form densely-packed regions relative to the systems with high solids levels. We see such an effect broadly in Fig. 4, where clearly densified regions are visibly more prevalent in the 25% and 30% solids systems than at higher solids levels. At higher solids levels, the structures of the aggregates are much more open and resemble fractal clusters formed by solid colloids[36,40,45] and adhesive

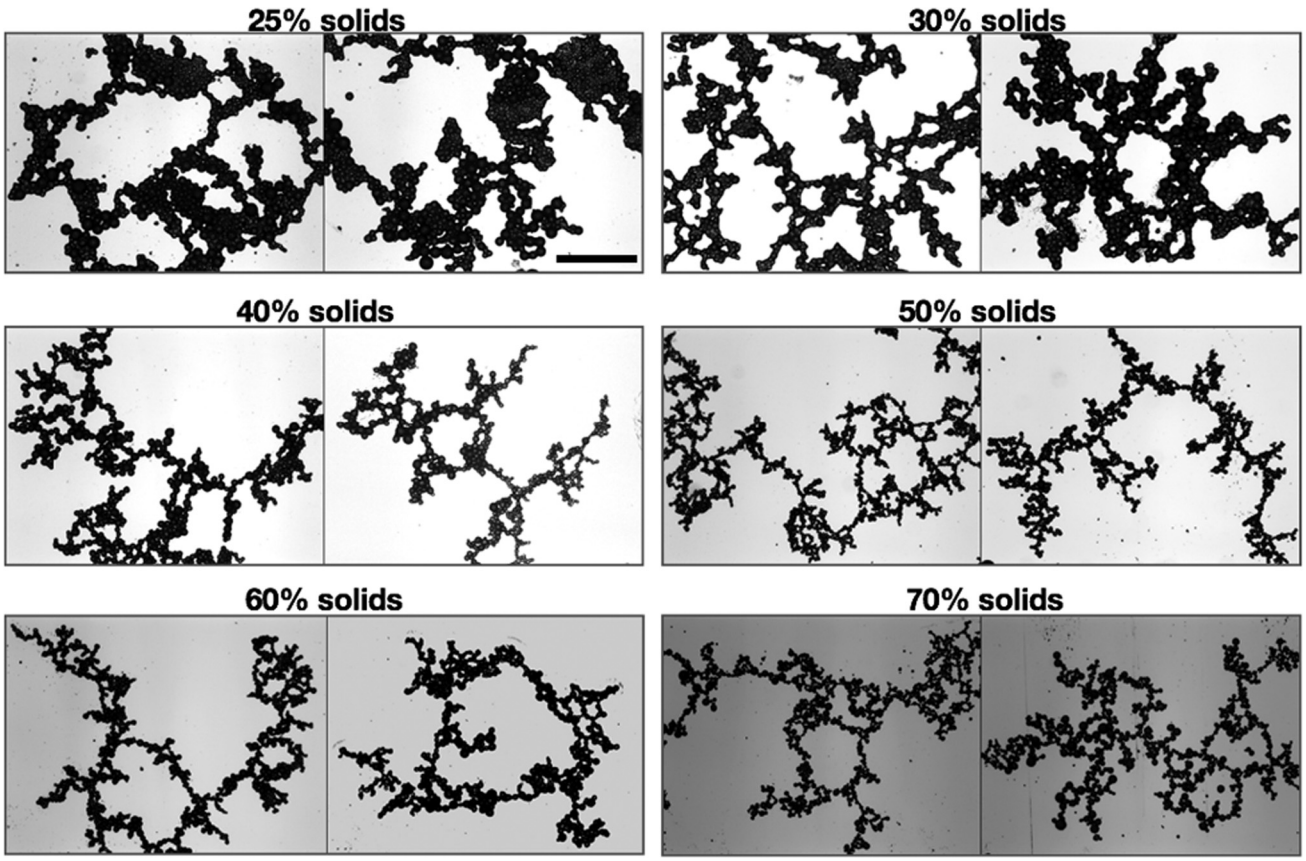

Fig. 4 Experimental aggregates. Micrographs of droplet aggregates formed at 25%, 30%, 40%, 50%, 60%, and 70% solid paraffin levels. As solids levels increase, droplets become increasingly open and linear in structure as the regions of close-packed droplets are reduced significantly. Scale bar is 2 mm.

emulsions.[43] Just as propagation-driven coalescence[29] exhibits evidence of the rearrangement observed in three-droplet systems,[17] the mechanism seems equally plausible for the flow-driven systems here with >1000 droplets, though the high speed of formation limits our ability to directly study kinetic assembly.

Fig. 5 shows close-up views of droplet aggregates at 25% and 30% solids concentrations. Increasing the solids level increases the droplet elasticity[14] and decreases the amount of free liquid oil available to restructure new droplets added to aggregates.[17] As seen above in Fig. 4, the reduced driving force for restructuring at increased solids levels creates aggregates with smaller regions of close-packed structure. The close-up views in Fig. 5 show the two main types of structures formed within these aggregates. Magenta arrows indicate regions at both concentrations where linear chains of single droplets are connected to form branches in the aggregate, just as might be seen in a typical fractal aggregate of solid particles.[37,46] Green arrows indicate regions where restructuring has clearly occurred and the droplets are arranged in close-packed forms.

We now test the predictions of the above model by comparing with experimental images of aggregates with different solids level. Past experimental studies of two-dimensional aggregate formation in well-controlled conditions noted two main regimes of behavior, characterized by the aggregate fractal dimension, D. Diffusion-Limited Aggregation, DLA, which we hypothesize occurs in this study, produces a fractal dimension, D = 1.66 while Reaction-Limited Aggregation (RLA) forms more compact aggregates with a higher fractal dimension than the DLA case.[39]

The value of aggregate D is typically determined in three different ways,[40] (i) a scaling relation between the mass and radius of gyration of clusters; (ii) a box-counting method and (iii) from the density–density correlation function $g(r)$. The scaling approach is not accessible to us, as we are able to observe only the final clusters, but we discuss below our use of $g(r)$ and box counting to determine the D as a function of droplet solid fraction.

The density–density correlation function $g(r)$ was calculated as follows: first, droplet centroid coordinates $\mathbf{x}_i$ were manually identified with ImageJ; the image was then binarized and extraneous droplets and artefacts removed. For each droplet i, the single particle correlation function, $g_i(r)$, was obtained by masking the binarized image of the aggregate with a filter containing an annulus of radius r and width dr, centered on $\mathbf{x}_i$ and counting the number of dark pixels as a function of r; these values are normalized by the area of each annulus. The quantity $g(r)$ is then calculated as $g(r) = \frac{1}{N}\sum_i g_i(r)$.

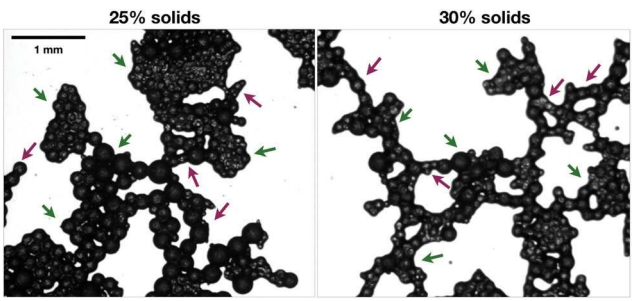

Fig. 5 Aggregate micro-environments. Close-ups of regions from Fig. 4 for 25% and 30% w/w solids showing regions of linear chain packing (magenta arrows) and close-packed regions of droplets (green arrows).

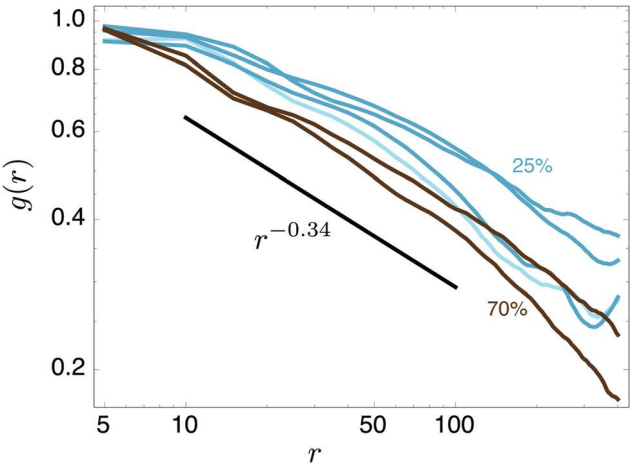

Fig. 6 Experimental density–density correlation function $g(r)$ calculated from aggregates containing 25%, 30% and 70% solids. The power-law $r^{-0.34}$ predicted for diffusion limited aggregation and the modified model discussed above is shown for comparison.

Results are shown in Fig. 6 for several aggregates with different solids level. While the experimental aggregates are fairly small, spanning from $500 \lesssim N \lesssim 1000$, they all display evidence for power-law behavior. Also plotted is a line $\propto r^{-0.34}$ predicted from the modified DLA model. Aggregates with high solids level (brown lines), which most clearly resemble dendritic DLA aggregates because of a lack of rearrangement, show the best agreement with this power-law. Those with a low solid fraction (darker blue lines) show weaker agreement, with a slightly shallower exponent, α. Further, there is some deviation from power-law behavior, particularly at longer length scales, indicating the possibility of additional structure.

Given the rapid process by which the aggregates form and are transported along the interface of the host droplet, it is remarkable that all of these aggregates, which are visually very distinct, show such relative consistency with the above prediction that the fractal dimension should be unaffected by marginal rearrangement events; it is possible that the additional structure at long length scales may be picked up in the latter phase of the formation process, where branches of the aggregate could shift positions closer to one another.

Fractal dimensions determined by $g(r)$ and box counting are plotted as a function of droplet solids level in Fig. 7A and B, respectively. In each case, D decreases with increasing solids level, consistent with our expectation that increasingly elastic droplets are less able to rearrange during collisions and arrest.[17] The mean values obtained from both techniques are listed in Table 1, and we observe some differences between the results returned by the two methods. The box counting fractal dimensions vary from D = 1.7–1.55 as a function of solid

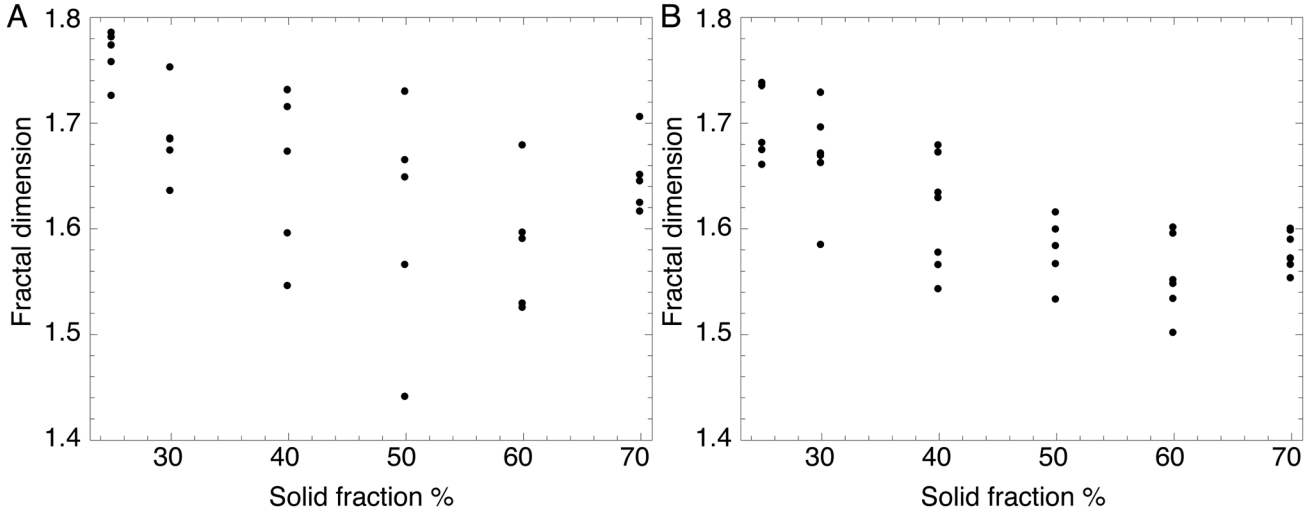

Fig. 7 Experimental fractal dimensions D as a function of solid fraction calculated from (A) $g(r)$ and (B) box counting.

Table 1 Mean fractal dimension D as a function of solid fraction measured by $g(r)$ and box counting methods. Quoted error is the standard deviation of measurements

Solids (%)	$g(r)$	Box counting
25	1.76 ± 0.02	1.70 ± 0.04
30	1.69 ± 0.04	1.67 ± 0.05
40	1.65 ± 0.08	1.61 ± 0.05
50	1.61 ± 0.11	1.58 ± 0.03
60	1.58 ± 0.06	1.55 ± 0.04
70	1.65 ± 0.04	1.58 ± 0.02

fraction, while those measured by $g(r)$ are overall around 0.1 higher. Nonetheless, both measures show a clear trend in Fig. 7: D falls by around 0.1 as solids levels go from 25% to 70%. We therefore cannot conclusively determine whether our experiments are in the RLA or DLA regime, but it is certainly possible that kinetics play a role in this variation as well as more complex combinations of capillary forces.[47]

We next turn to evaluating structure *via* the characteristic contact number using the droplet centroids $\{\mathbf{x}_i\}$. In the theoretical calculation plotted in Fig. 3C, the droplets are uniformly sized and exhibit a clear length scale λ on which a contact may be defined: two particles i and j are said to be in contact if $|\mathbf{x}_i - \mathbf{x}_j| < \lambda$. Below this length scale, no contacts are detected, while the number of contacts diverges as $\lambda \gg R$.

Experimentally, the droplets are somewhat polydisperse, and no single length scale can be used to identify contacts. To circumvent this challenge, we adapt a technique common in the jamming community to analyze contact networks.[48] First, we define a probe ball around each particle with radius λ, illustrated as an inset in Fig. 8A, and count any particle that intersects with the probe ball as a contact. By placing the probe

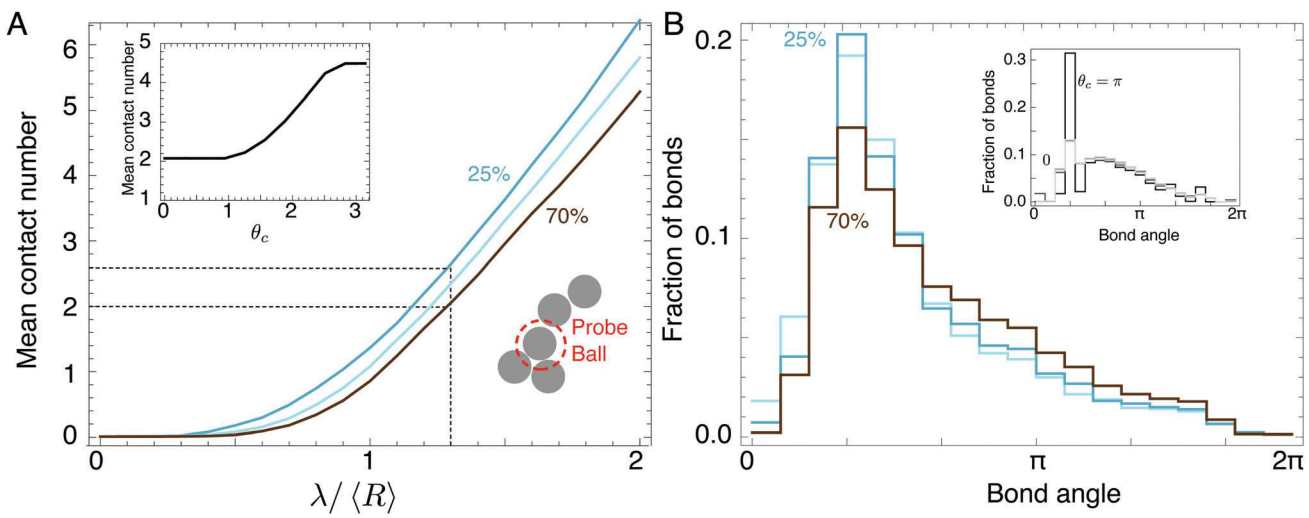

Fig. 8 (A) Mean contact number of experimental aggregates as a function of probe radius λ, scaled by the mean droplet radius $\langle R\rangle$ for different solid level. Dashed lines are a guide to the eye. Inset: Theoretical mean contact number calculated from the model. (B) Distribution of angles between neighboring contacts for different solid fraction. Inset: Distributions for θ_c = 0, π/3, 2π/3, and π from simulated aggregates.

ball around the centroid of a particle, we can count the number of contacts found for a given λ and hence compute the contacts per particle, $Z(\lambda)$, as depicted in Fig. 8A.

We display for different solid fractions in Fig. 8A the mean contact number $Z(\lambda)$ as a function of λ scaled by the mean droplet radius $\langle R \rangle$. These plots show a smooth transition from under-counting as $\lambda \to 0$ to over-counting as $\lambda \gg \langle R \rangle$, but regardless of the value of λ chosen, the conclusion is the same: droplets with 25% solids level possess, on average, 0.6 additional contacts per droplet *versus* the 70% solids case. This is consistent with our observations of Fig. 4, where lower solids level droplets have a greater number of compact-packing regions than their higher solids level counterparts. The result also agrees nicely with past experimental work showing a clear increase in restructuring for droplets with decreased solids levels.[17]

Visual inspection of the contacts selected suggests that a value of $\lambda \sim 1.3$ corresponds with observable bridging between particles; this value is indicated in the plot with dashed lines. At such a value of λ, the mean contact number per droplet for the 70% solids level is around $Z = 2$. To compare this with the modified DLA model, the mean contact number per particle is shown as a function of the critical angle for restructuring, θ_c. The experimentally observed value of $Z = 2$ corresponds to $\theta_c \lesssim \pi/3 \approx 1$. Decreasing the solid level to 25% increases the mean contact number to $Z = 2.6$, which would imply a critical angle of $\theta_c = 1.6 \approx \pi/2$. A small variation in solids level, to 30%, leads to a large change in mean contact number, $Z = 2.3$, which would imply $\theta_c \sim 1.3$ rad or 0.4π. Although past study of individual three-droplet aggregates found a similar trend: reduction in critical angle with decreased solids levels,[17] the values found here are lower than the experimental critical angles. The previous study found a critical angle $\theta_c \approx 2\pi/3$ for droplets containing 25% solids and $\theta_c > 2\pi/3$ for solids levels less than 25%. This discrepancy is likely due to contributions of flow that we can not yet account for with our microscopy study or simulations. Flow could influence whether rearrangement occurs during a collision, as the incoming momentum of the droplet could, for example, act in concert with the capillary force to enhance rearrangement likelihood. The complex combination of directional forces will ultimately determine whether rearrangement occurs, but we are not yet able to quantify these factors in our experiments or simulations. This will be a focus of future work.

Another measure of local structure in the aggregates is the distribution of bond angles between droplets, and these values are plotted in Fig. 8B for the experimental system and the simulation. Because capillarity-induced rearrangements move droplets into a close-packed state, we expect to see an increase in droplets with bond angles of $\pi/3$ if rearrangement is significant. Fig. 8B compares distributions for the experimental aggregates, and we see a clear decrease in large bond angles, and an increase in bond angles of $\pi/3$ as solids levels increase. Our simulation results, plotted as inset in Fig. 8B, also show an increase in bond angles of $\pi/3$, but only for $\theta_c = \pi$.

Consistent with previous work on three-droplet systems,[17] we see that the connectivity in a flow-induced arrested network of many droplets can be adjusted by altering the likelihood of capillarity-driven restructuring. The model indicates a potentially promising approach to larger-scale simulation of aggregates restructured by this unique mechanism and insight into their bulk mechanical and transport properties.

4 Conclusions

We studied two-dimensional droplet network formation when arrest or aggregation dominates coalescence. The results provide support for the hypothesis that droplet rearrangement mechanisms found in past studies of three-droplet systems may also occur in many-droplet networks. The work provides a basis for simulation of arrested coalescence by adding new quantitative mechanisms of structural rearrangement, enabling prediction of more complex systems in two and three dimensions. An understanding of the packing and connectivity within such structures is critical to predicting mechanical properties and dynamic performance of materials as diverse as foods, cosmetics, and 3D printed products. The work also demonstrates a new aspect of responsiveness and shape-change: rearrangement of an underlying elastic framework using the strong driving force of a liquid interface.[49] We show that numerous complex shapes can be self-assembled even from simple droplet building blocks larger than the thermal limit. We envision increased complexity in systems where droplet shape is non-spherical and rearrangement is significant,[25] providing additional means of self-assembly control. Dynamic shape change using physical mechanisms, like geometry and interfacial driving forces,[50] will be a critical aspect of future directed and active material assembly efforts at the nanoscale,[51] where Brownian motion is significant, as well as at the microscale, where thermal motion no longer dominates.

Conflicts of interest

There are no conflicts to declare.

Acknowledgements

This material is based upon work supported by the National Science Foundation under grant DMR-1654283. The authors also acknowledge partial support from the Australian Government through the Australian Research Council's Discovery Projects funding scheme, Project DP150100865.

Notes and references

1 H. D. Goff, *Int. Dairy J.*, 1997, **7**, 363–373.
2 D. Rousseau, *Food Res. Int.*, 2000, **33**, 3–14.
3 I. Heertje, *Food Struct.*, 2014, **1**, 3–23.
4 K. Boode and P. Walstra, *Colloids Surf., A*, 1993, **81**, 121–137.
5 E. Fredrick, P. Walstra and K. Dewettinck, *Adv. Colloid Interface Sci.*, 2010, **153**, 30–42.

6 M. Caggioni, D. Traini, P. M. Young and P. T. Spicer, *Powder Technol.*, 2018, **329**, 129–136.
7 M. Caggioni, A. Bayles, J. Lenis, E. Furst and P. Spicer, *Soft Matter*, 2014, **10**, 7647–7652.
8 M. Caggioni, J. Lenis, A. V. Bayles, E. M. Furst and P. T. Spicer, *Langmuir*, 2015, **31**, 8558–8565.
9 P. Spicer, M. Caggioni, J. Lenis and A. Bayles, Shape-Changing Droplet, *Eur. Pat.*, 2909299B1, Procter and Gamble Co., 2017.
10 P. Spicer, M. Caggioni, J. Lenis and A. Bayles, Non-Spherical Droplet, *US Pat.*, 9597648, Procter and Gamble Co., 2017.
11 T. A. Prileszky, B. A. Ogunnaike and E. M. Furst, *AIChE J.*, 2016, **62**, 2923–2928.
12 T. A. Prileszky and E. M. Furst, *Langmuir*, 2016, **32**, 5141–5146.
13 T. A. Prileszky and E. M. Furst, *Chem. Mater.*, 2016, **28**, 3734–3740.
14 A. Pawar, M. Caggioni, R. Hartel and P. Spicer, *Faraday Discuss.*, 2012, **158**, 341–350.
15 P. Dahiya, M. Caggioni and P. T. Spicer, *Philos. Trans. R. Soc., A*, 2016, **374**, 20150132.
16 A. E. Thiel, R. W. Hartel, P. T. Spicer and K. J. Hendrickson, *J. Am. Oil Chem. Soc.*, 2016, 1–11.
17 P. Dahiya, A. DeBenedictis, T. J. Atherton, M. Caggioni, S. W. Prescott, R. W. Hartel and P. T. Spicer, *Soft Matter*, 2017, **13**, 2686–2697.
18 R. F. Visintin, T. P. Lockhart, R. Lapasin and P. D'Antona, *J. Non-Newtonian Fluid Mech.*, 2008, **149**, 34–39.
19 J. N. Coupland, *Crystallization of Lipids: Fundamentals and Applications in Food, Cosmetics, and Pharmaceuticals*, 2018, p. 431.
20 F. Thivilliers, R. Backov, V. Schmitt and F. Leal-Calderon, *Langmuir*, 2007, **23**, 4792–4799.
21 F. Thivilliers, E. Laurichesse, F. Leal-Calderon and V. Schmitt, *Langmuir*, 2008, **24**, 13364–13375.
22 F. Thivilliers-Arvis, E. Laurichesse, V. Schmitt and F. Leal-Calderon, *Langmuir*, 2010, **26**, 16782–16790.
23 S. S. Narine and A. G. Marangoni, *Food Res. Int.*, 1999, **32**, 227–248.
24 A. G. Marangoni, *Trends Food Sci. Technol.*, 2002, **13**, 37–47.
25 C. Hao, Z. Xie, T. J. Atherton and P. T. Spicer, *Langmuir*, 2018, **34**, 12379–12386.
26 C. Aubert and D. S. Cannell, *Phys. Rev. Lett.*, 1986, **56**, 738.
27 W. Y. Shih, I. A. Aksay and R. Kikuchi, *Phys. Rev. A: At., Mol., Opt. Phys.*, 1987, **36**, 5015.
28 J. Stankiewicz, M. A. C. Vlchez and R. H. Alvarez, *Phys. Rev. E: Stat. Phys., Plasmas, Fluids, Relat. Interdiscip. Top.*, 1993, **47**, 2663.
29 S. Abedi, N. S. Suteria, C.-C. Chen and S. A. Vanapalli, *J. Colloid Interface Sci.*, 2019, **533**, 59–70.
30 Z. Varga, G. Wang and J. Swan, *Soft Matter*, 2015, **11**, 9009–9019.
31 P. Padmanabhan and R. Zia, *Soft Matter*, 2018, **14**, 3265–3287.
32 G. Wang and J. W. Swan, *Soft Matter*, 2019, **15**(25), 5094–5108.
33 M. Bouzid and E. Del Gado, *Langmuir*, 2017, **34**, 773–781.
34 B. A. Schultz, P. F. Damasceno, M. Engel and S. C. Glotzer, *ACS Nano*, 2015, **9**, 2336–2344.
35 C. A. Schneider, W. S. Rasband and K. W. Eliceiri, *Nat. Methods*, 2012, **9**, 671–675.
36 S. Reynaert, P. Moldenaers and J. Vermant, *Langmuir*, 2006, **22**, 4936–4945.
37 T. Witten Jr and L. M. Sander, *Phys. Rev. Lett.*, 1981, **47**, 1400.
38 T. A. Witten and L. M. Sander, *Phys. Rev. B: Condens. Matter Mater. Phys.*, 1983, **27**, 5686.
39 A. J. Hurd and D. W. Schaefer, *Phys. Rev. Lett.*, 1985, **54**, 1043.
40 D. Robinson and J. Earnshaw, *Phys. Rev. A: At., Mol., Opt. Phys.*, 1992, **46**, 2045.
41 R. Jullien and P. Meakin, *J. Colloid Interface Sci.*, 1989, **127**, 265–272.
42 M. Cavallaro, L. Botto, E. P. Lewandowski, M. Wang and K. J. Stebe, *Proc. Natl. Acad. Sci. U. S. A.*, 2011, **108**, 20923–20928.
43 J. Bibette, T. Mason, H. Gang, D. Weitz and P. Poulin, *Langmuir*, 1993, **9**, 3352–3356.
44 R. A. Letteri, C. F. Santa Chalarca, Y. Bai, R. C. Hayward and T. Emrick, *Adv. Mater.*, 2017, **29**, 1–8.
45 D. A. Weitz and M. Oliveria, *Phys. Rev. Lett.*, 1984, **52**, 1433–1436.
46 M. Y. Lin, H. M. Lindsay, D. A. Weitz, R. C. Ball and P. Meakin, *Phys. Rev. A: At., Mol., Opt. Phys.*, 1990, **41**, 2005–2020.
47 B. J. Park and E. M. Furst, *Soft Matter*, 2011, **7**, 7676–7682.
48 Z. Xie, C. J. Burke, B. Mbanga, P. T. Spicer and T. J. Atherton, *Soft Matter*, 2019, **15**, 9587–9596.
49 C. Py, P. Reverdy, L. Doppler, J. Bico, B. Roman and C. Baroud, *Phys. Rev. Lett.*, 2007, **98**, 156103.
50 J.-P. Péraud and E. Lauga, *Phys. Rev. E: Stat., Nonlinear, Soft Matter Phys.*, 2014, **89**, 043011.
51 J.-H. Cho, T. James and D. H. Gracias, *Adv. Mater.*, 2010, **22**, 2320–2324.